Multi-Objective optimization of an IGV for a large axial fan based on NSGA-II

Shuiqing Zhou[1,2]*, Tianle Zhang[1,2], Zijian Mao[1,2] and Laifa Lu[1,2]

[1]College of Mechanical Engineering, Zhejiang University of Technology, Hangzhou, Zhejiang, China, [2]Institute of Innovation Research of Shengzhou, Zhejiang University of Technology, Shengzhou, Zhejiang, China

Large axial fans are widely used in industrial refrigeration, building ventilation, and other scenarios because they have inlet guide vanes (IGVs) and outlet guide vanes (OGVs) to make their operation economical and efficient. However, unreasonable guide vane structure is prone to flow separation, forming a tail vortex and interfering with other blades, thereby resulting in the deterioration of working conditions and large noise. Taking a large axial fan with both IGVs and OGVs as the research object, this paper analyzed the structural variables of the fan by global sensitivity analysis method and determine the target of settings optimization as IGV according to the analysis results and the internal flow characteristics of the fan. Furthermore, IGV was parametrically designed, and Kriging model was established and optimized by the second non-dominated sorting genetic algorithm (NSGA-II). Eventually, total pressure and sound pressure level (SPL) were used as targets for multi-objective optimization. The results indicated that the noise produced by the optimized fan was reduced by 6.4 dB and total pressure was increased by 156.4 Pa, with an increase of 0.86% in the total pressure efficiency at the rated working condition, which proved the reliability of the proposed method. This paper also provides a valuable reference for the optimization of similar fluid equipment.

1 Introduction

Blades are the core components of large axial fans, which are crucial to the aerodynamic noise and performance characteristics as well as the safe and stable operation of the fans (Zhao et al., 2020; Gu et al., 2021). A large nuclear-grade axial fan with a diameter of 1250 mm was used as the research object of this study. It is generally used in the ventilation system of nuclear power plants, working at medium pressure, with Mach <0.3 and Reynolds >4000. At this time, potential dangers in the internal flow field of the blade is likely to obstruct fluid flow, affect the efficiency of the fan and even damage motor, which will endanger stable operation and lead to equipment damages or power

plant shutdown, and thus huge economic losses and adverse social impact (Zhang et al., 2018; Fakhraei et al., 2021). Therefore, it is of great urgency to optimize the fan.

Since the fans under study are used in ventilation systems, huge noise generated during operation would have an impact on the health of nearby personnel (Zhang C. et al., 2021), so optimization objective is to simultaneously increase pressure and reduce noise, which is quite difficult to achieve (Hu and Lu, 2017; Kromer et al., 2019). And it cannot be achieved by increasing the size of the fan because of its large size and complex structure, nor can it be achieved by the traditional methods. In addition, with the implementation of China's carbon neutrality and carbon peaking policies, the energy efficiency ratio of the equipment is becoming increasingly important (Tanasic et al., 2011; Huang et al., 2020). In this context, it is vital to find a way to simultaneously increase pressure and reduce noise without increasing fan size and power consumption. One of the most important methods is to optimize the structure of the fan.

The structural optimization of axial flow fans has been studied by many outstanding scholars. KIM et al. (Kim et al., 2014) used a weighted average proxy model to optimize the design with a single objective for five design variables and performed multi-objective optimization on this basis to improve efficiency while reducing SPL. CANEPA E et al. (Canepa et al., 2016) investigated the tip leakage noise generated by a shrouded rotor of an axial fan and calculated the acoustic response function of the tested configuration using the spectral decomposition method. The findings showed that upstream geometry had a more significant effect on radiated noise than on performance and that a sharp decline in tip-gap failed to entirely eliminate relevant noise. ZHANG (Zhang S. G. et al., 2021) used a single-stage axial fan based on the radial basis function (RBF) enhanced differential evolutionary (RADE) algorithm to conduct dual-objective optimization with power consumption and static pressure efficiency as the design objectives. The results suggested an increase of 6% in the static pressure efficiency of the axial fan and a decrease of 7 dB in the first blade pass frequency (BPF) noise after optimization.

Nowadays, approximate models are mostly used for the optimization of fan structures to reduce computational effort and improve efficiency. CHOI et al. (Choi et al., 2019) applied the response surface method (RSM) based on central composite design for single objective optimization to enhance the aerodynamic performance at a specified total pressure, and the optimization results showed an increase in the total pressure and efficiency of 5.2% and 2.0% respectively. Using gradient enhanced response surface model (GERSM), TANG et al. (Tang et al., 2017) optimized the aerodynamic shape of a transonic fan and gave the geometric characteristics and relevant details of the optimal design. NISHI et al. (Nishi et al., 2022) applied a one-dimensional design approach to a very small axial fan by combining experimental design, response surface method

(RSM) and optimization method and eventually succeeded in improving the efficiency of the fan by about 9.1% through numerical analysis and experiments.

Despite various approximate models have been used for the structural optimization of fans, most of the studies have clear objectives, and the studied structures are single-stage blades with fewer influencing factors (Venturelli and Benini, 2016; Chai et al., 2020; Taghinezhad et al., 2021). In addition, sensitivity analysis is rarely performed. Therefore, based on a preliminary investigation (Zhou et al., 2022), this paper optimized the complex structures of large axial fans and analyzed the responsivity of multiple influencing factors to pressure and noise by using global sensitivity analysis method and combining the research results and the internal flow characteristics of the fans to determine the structure after verifying the feasibility of numerical simulations. On this basis, Kriging model with relevant optimization variables and target response was established and optimized by NSGA-II with pressure and noise as the target. Finally, the optimization results were verified by air performance and noise tests. The above method is also applicable to the optimal design of other fans with complex structures such as multi-stage blades and similar machinery, which have certain reference and application value.

2 Numerical simulation analysis and verification

2.1 Research objects

A large axial fan mainly consists of a fairing, IGVs, moving vanes, OGVs, and a motor, as shown in Figure 2.

Structural parameters are shown in Table 1.

2.2 Computational model and verification

To facilitate the calculation of the internal component area and grid division of the fan, the geometric model of the fan was divided into five components, namely inlet, IGV, rotation, OGV, and outlet, whose simplified diagram is shown in Figure 3.

Figure 4 shows grid delineation. The important parts (moving vanes, IGVs, OGVs) were structurally meshed to improve the mesh quality. The meshes of IGV, rotation and OGV grids are respectively displayed in Figures 4B–D. The complete fan grid is shown in Figure 4A. In this case, the first node was placed in the region of the viscous substratum with y+ ≤ 5. The Y^+ empirical formula is expressed as Eq. 1 (Moaveni, 1999):

$$Y_{wall} = 6\left(\frac{V_{ref}}{\nu}\right)^{-\frac{7}{8}}\left(\frac{L_{ref}}{2}\right)^{\frac{1}{8}}y^+ \qquad (1)$$
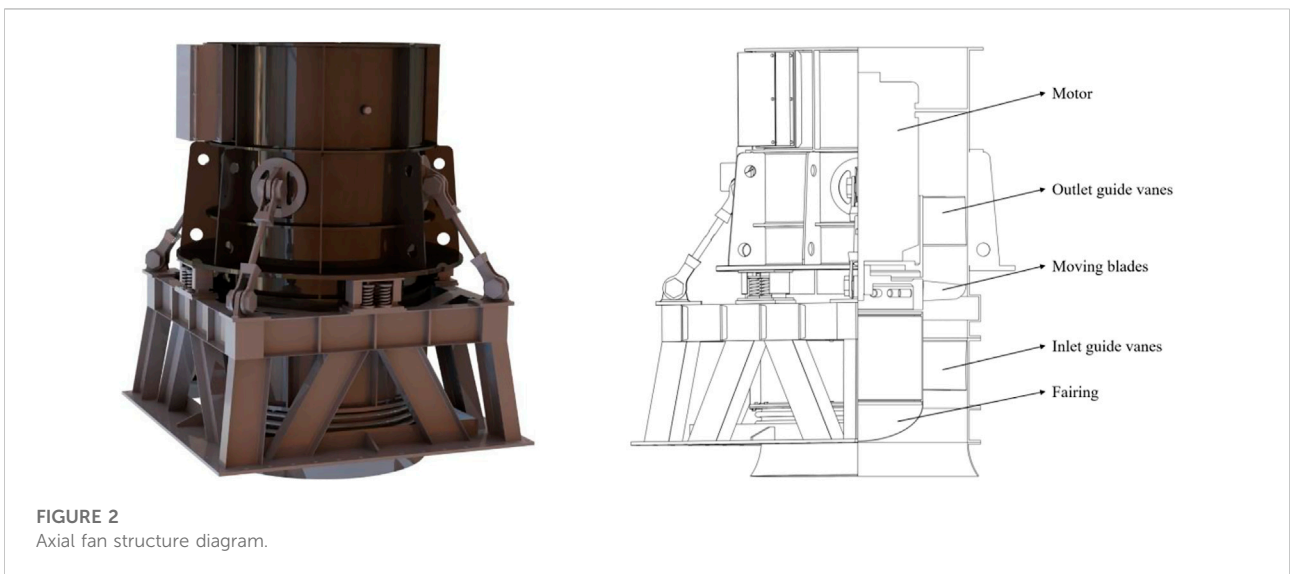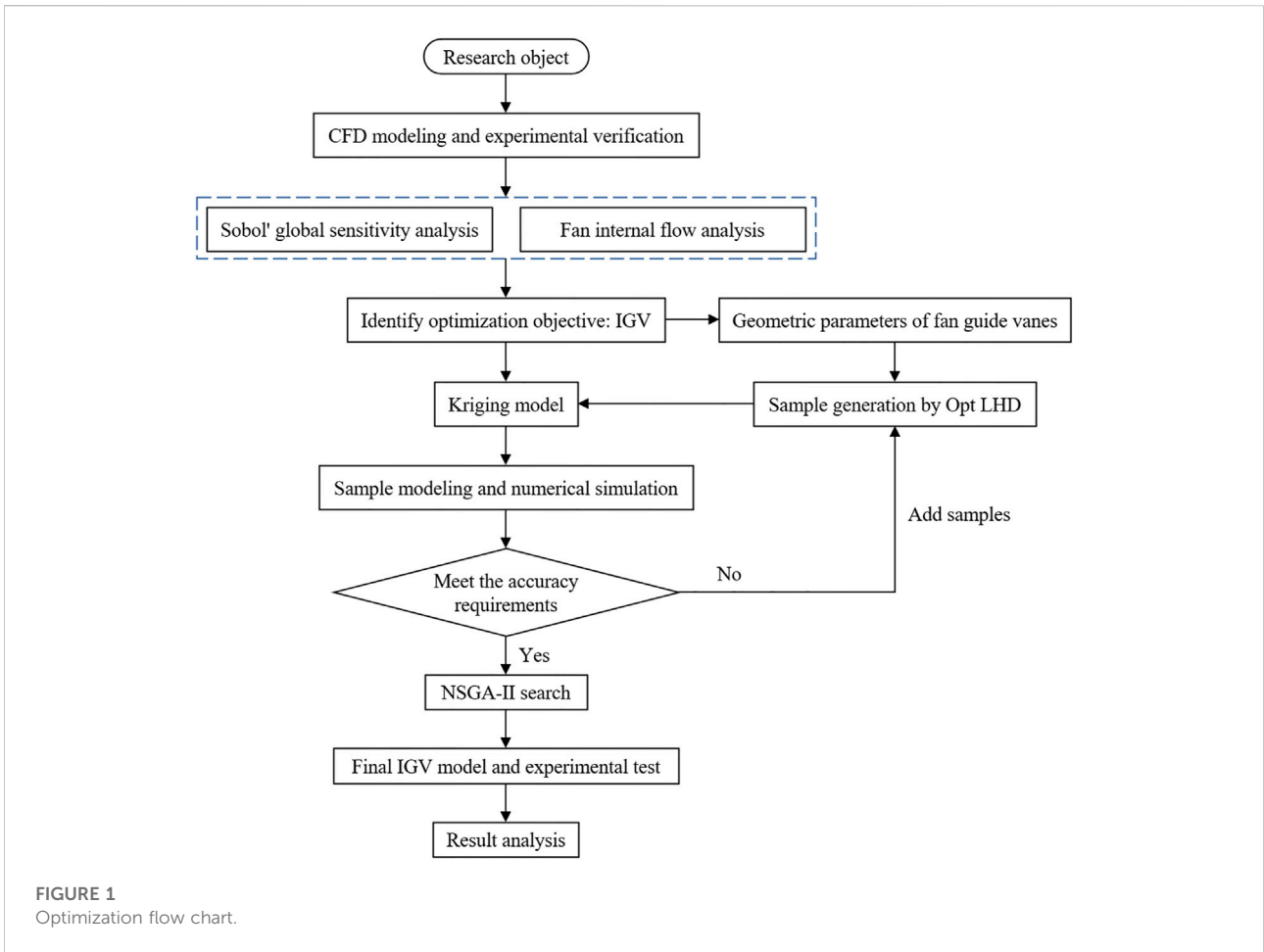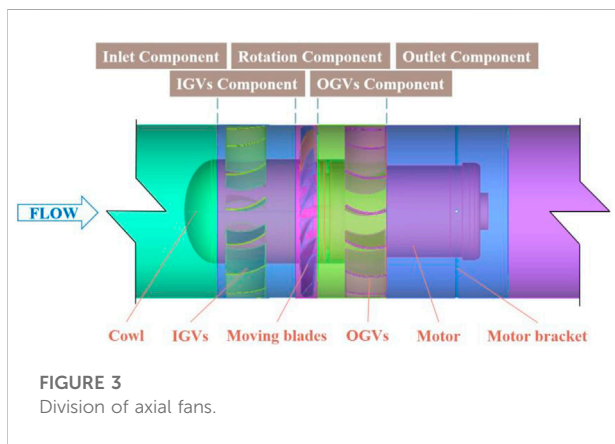
FIGURE 1
Optimization flow chart.

FIGURE 2
Axial fan structure diagram.

TABLE 1 Structural parameters of axial flow fan.

Parameter	Symbol	Numerical value	unit
Diameter	D	1250	mm
IGVs number	m_1	15	pieces
Number of moving Blades	Z	14	pieces
OGVs number	m_2	15	pieces
Rotating speed	n	1485	r/min
Flow rate	Q	82,400	m³/h
Total pressure (25°C)	p_{tf}	2300	Pa
Noise SPL (25°C)	SPL	111.7	dB

FIGURE 3
Division of axial fans.

Grid independence was verified after grid division, as demonstrated in Figure 5. When there were a total number of about 8×10^6 grids, the total pressure of the fan obtained from numerical simulation remained unchanged, while its total pressure efficiency fluctuated by less than 1%, then the calculation results were believed to be independent of the number of grid. At this time, there were 8,267,684 grids in the whole fan component in total.

To verify the accuracy of the computational model, the aerodynamic performance and noise of the fan was numerically and experimentally simulated. Then the simulation and experimental results were compared and analyzed. The pressure of the fan was simulated on the computational model. The steady-state calculation was conducted using the multi-reference system model (MRF). To solve the implicit pressure-based solution, the standard k-ε turbulence model was used to solve the three-dimensional Reynolds-averaged N-S equation, the working fluid was 25°C air, and the inlet and outlet boundary conditions were set to Mass-flow-inlet and Pressure-outlet. The SIMPLE algorithm was employed couple pressure and velocity, with each exponential parameter of aerodynamic performance being set to second-order headwind. However, Under-Relaxation factors were set by default.

The calculation converged when the residual value was less than 1×10^{-5}.

According to the requirements of "GB/T 1236–2017 duct industrial ventilator standardized duct performance test" (General Administration of Quality Supervision, 2017) for fan aerodynamic test, a C-type air chamber was adopted. The schematic diagram of air performance test and field experimental setup is shown in Figures 6A,B. The performance of the fan was tested at room temperature and pressure, air parameters corresponding to various operating conditions of the axial fan were recorded by a comprehensive atmospheric pressure, temperature and air humidity tester at the front of the inlet collector (wind speed was zero), and the opening and flow rate of the cylinder were regulated by the inlet throttling device. During the experiments, the inlet throttling device was adjusted to record the inlet and outlet pressures and the pressure difference between the Pitot tube and hydrostatic tube under ten sets of flow conditions.

Figure 6C compares the numerical simulation with experimental results. It can be seen from the figure that the simulated values of total pressure and efficiency were basically consistent with the experimental values. The simulated value of total pressure was slightly lower than the experimental value, with a maximum error of less than 5%. There was a small difference between the simulated and experimental values in terms of efficiency, with a maximum error of 9.09% at low flow rates and an error of less than 3% at the remaining positions. Therefore, the computational model is considered to be highly reliable.

Noise was simulated on the computational model using a large eddy combined with sound simulation theory. The steady flow field was firstly calculated and then used as the initial flow field for calculating the unsteady flow field. The far-field noise of the fan was determined in the commercial software by calculating the time-domain integral and area fraction. The time required to rotate the hub by 1° is represented by the time step Δt, where $\Delta t = 1/(6n)$. Therefore, in order to accurately obtain the information about near-field flow field, the time step was set to 0.0001 s in this study.

The sound field was calculated by fast Fourier transform (FFT) to determine the SPL and noise spectrum. The formula for solving the time domain for the instantaneous sound pressure p (Wu Chen and Zhou, 2021) is:

$$p' = \frac{1}{4\pi} \int_{f=0} \left[\frac{L_r}{r^2} \right] \mathrm{d}S + \frac{1}{4\pi} \int_{f=0} \left[\frac{\dot{L}_r}{r^2} \right] \mathrm{d}S \tag{2}$$
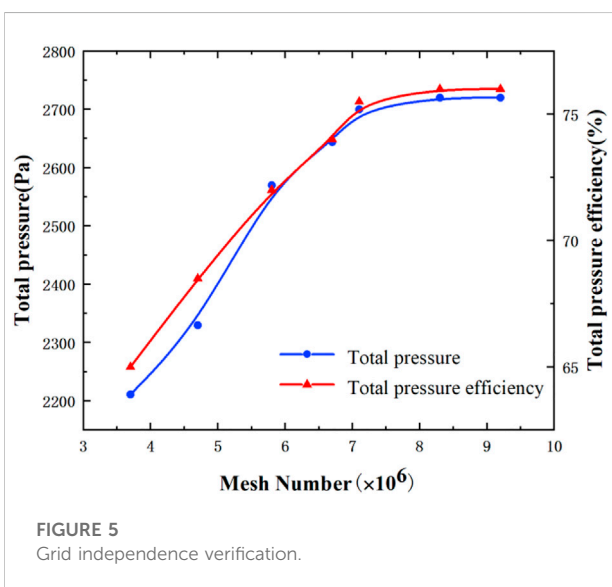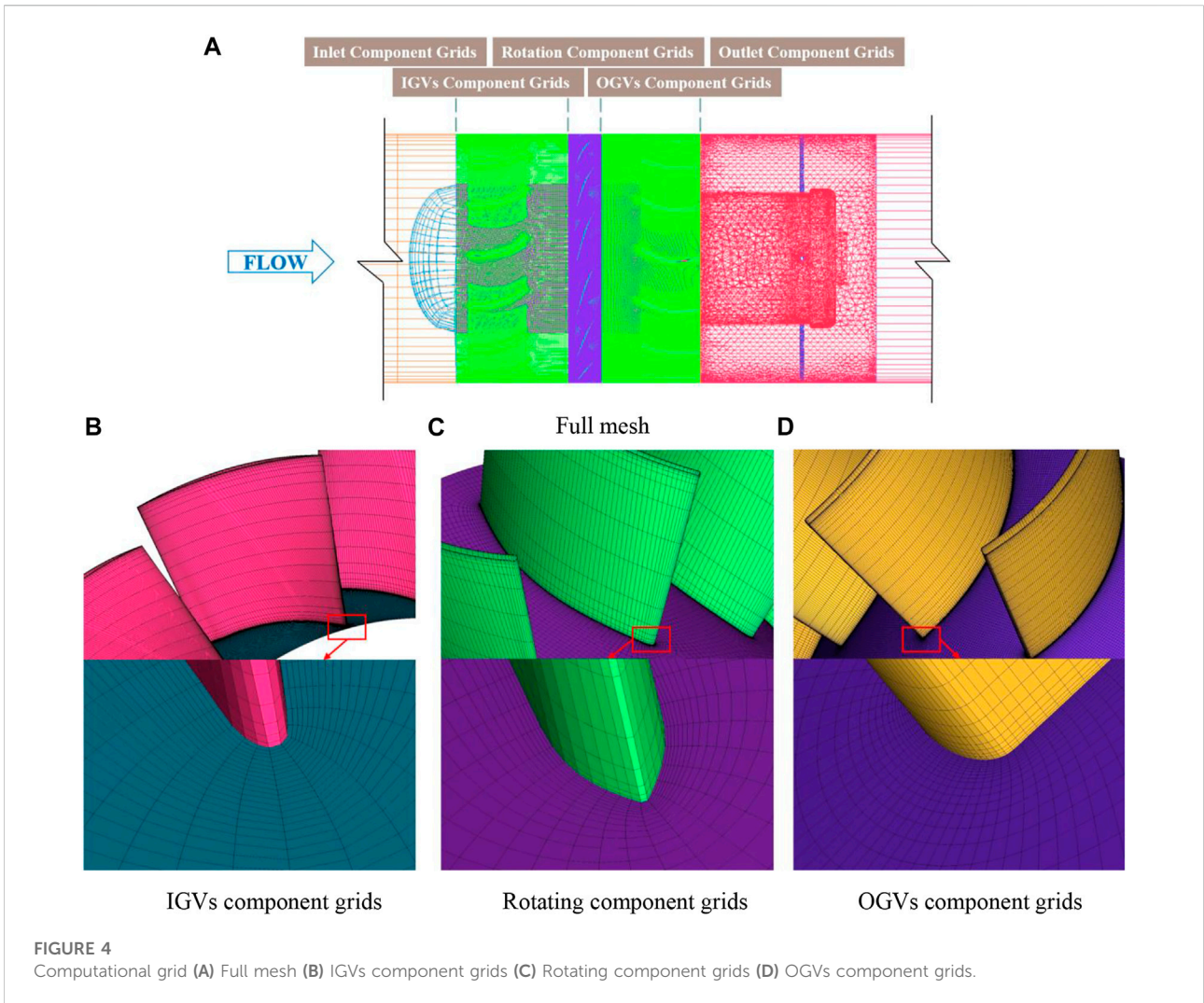
$$L_r = L_i \hat{r}_i \tag{3}$$

$$\dot{L}_r = \dot{L}_i \hat{r}_i \tag{4}$$

$$L_i = p n_i \tag{5}$$
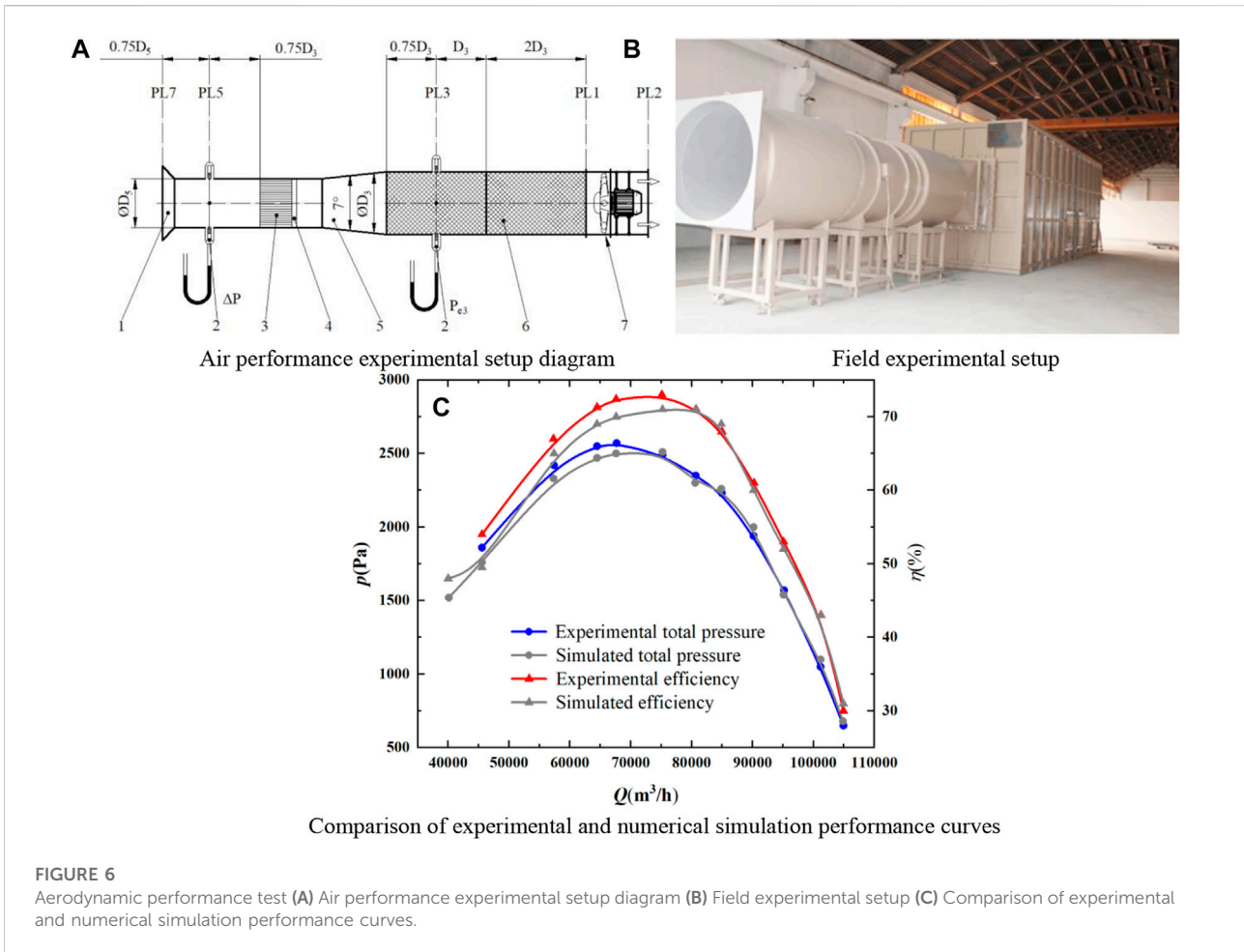
$$\hat{r}_i = \frac{x_i - y_i}{\sqrt{(x_i - y_i)^2}} \tag{6}$$

where r is the distance from the sound source to the receiving point, "·" represents the derivative of time, $\hat{r}_i$ represents the unit

FIGURE 4
Computational grid **(A)** Full mesh **(B)** IGVs component grids **(C)** Rotating component grids **(D)** OGVs component grids.

FIGURE 5
Grid independence verification.

vector from the sound source to the receiving point, n_i is the wall normal vector.

According to the noise test standard "GB/T2888-2008 Fan and Roots Blower Noise Measurement Method" (General Administration of Quality Supervision, 2008), the noise receiving point was set at 1,250 mm (diameter) at a horizontal position of 45° from the center of the outlet surface. The schematic diagrams of noise monitoring points and experimental settings are individually shown in Figures 7A,B.

Figure 7C shows the experimental and numerical simulation noise results. As can be seen from the figure, the fan was under extreme conditions at the flow rate of around 70,000 m³/h, whose simulated noise value was lower than the experimental one, with a maximum error of less than 3%. However, the two values tended to be consistent when the fan was working at the flow rate of more than 75,000 m³/h. And when the flow rate was close to the designed one, the average noise values during experiment and

FIGURE 6
Aerodynamic performance test **(A)** Air performance experimental setup diagram **(B)** Field experimental setup **(C)** Comparison of experimental and numerical simulation performance curves.

simulation were respectively 111.52 dB and 110.88 dB, with a relative error of ≤0.57%.

The above analysis demonstrates that the noise of the fan designed according to the standard of nuclear counting fan exceeded the requirements, with aerodynamic performance poorer than the standard, so it needed to be optimized. The fan is a non-standard design, with many structural components and interactional influencing factors, so it is of great importance to analyze these factors to identify the optimal optimization objective.

3 Determination of optimized structure

3.1 Global sensitivity analysis method and implementation method

A large number of influencing factors were involved in this study, and Sobol' global sensitivity analysis method was selected because it can quantify the input and output uncertainties as probability distributions and attribute the output variance to the combination between the input variables that fits better with the problem in this study.

Global sensitivity analysis (Hart and Gremaud, 2018) gives the relationship between the partial derivatives of the output concerning the input variables over the entire input variable space, i.e. $f(\theta) = \partial P_f(\theta)/\partial \theta|_{\theta \in \Theta}$, or a sensitivity indicator used to indicate the importance of the input variables and to rank the importance of the input variables, so it is also known as importance measure analysis.
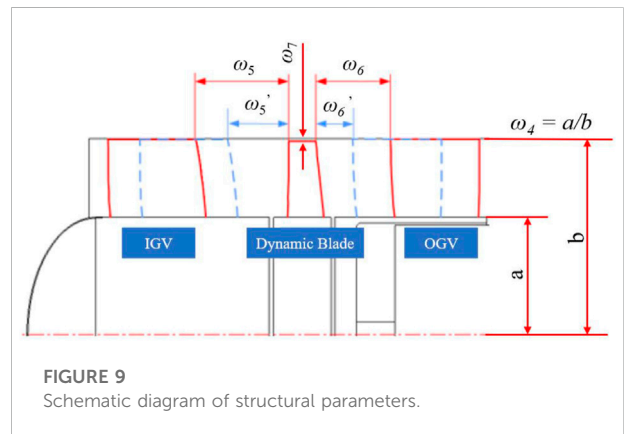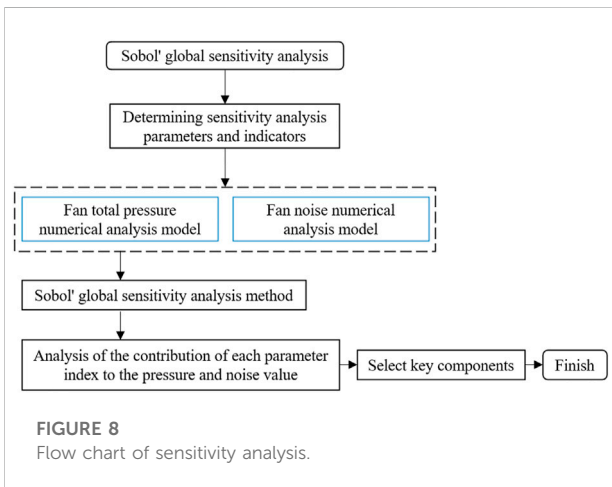
The global sensitivity metric S_i is defined (Cui et al., 2010) as:

$$S_i = \frac{V[E(I_F|x_i)]}{V(I_F)} \quad (7)$$

$$I_F(x) = \begin{cases} 1, x \in \text{Invalid Domain} \\ 0, x \notin \text{Invalid Domain} \end{cases} \quad (8)$$

$$V(I_F) = E(I_F^2) - E^2(I_F) = E(I_F) - E^2(I_F) \quad (9)$$

where $V(\cdot)$ is the variance operator, $E(I_F|x_i)$ is the mathematical expectation of the failure indicator function I_F under the

FIGURE 7
Noise test **(A)** Noise monitoring point settings **(B)** Noise experimental setup **(C)** Experimental and numerical simulation noise results.

FIGURE 8
Flow chart of sensitivity analysis.

FIGURE 9
Schematic diagram of structural parameters.
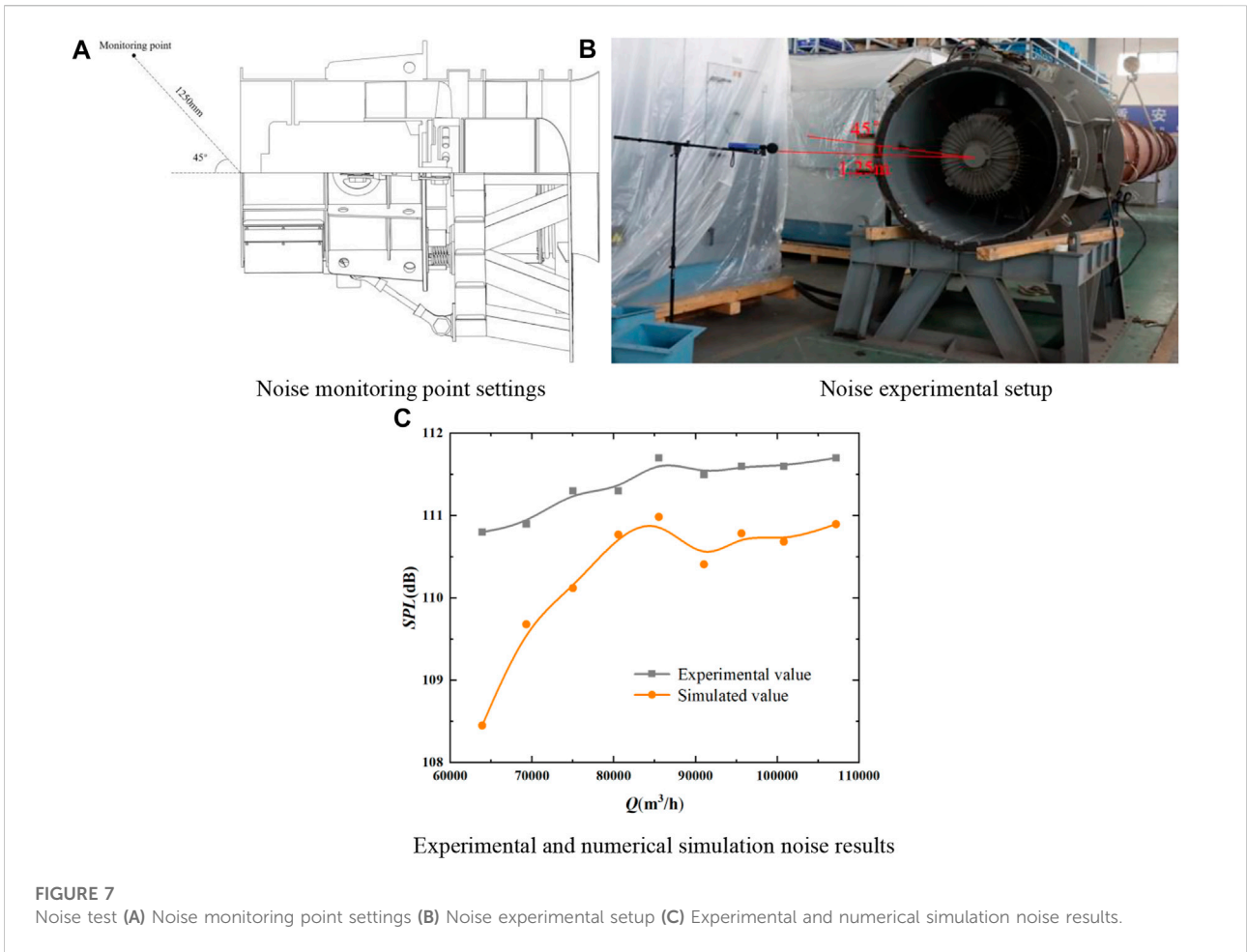
condition of random variable x_i, and I_F is the failure domain indicator function.

For some input variable x_i, the global sensitivity principal indicator is:

$$S_i = \frac{V[E(I_F|x_i)]}{V(I_F)} = \frac{E\left(E^2(I_F|x_i)\right) - E^2\left(E^2(I_F|x_i)\right)}{E(I_F^2) - E^2(I_F)} = \frac{E\left(E^2(I_F|x_i)\right) - E^2(I_F)}{E(I_F) - E^2(I_F)}$$

(10)

The fan mainly consisted of IGV, moving vane, OGV, etc. Therefore, a total of 14 parameters, namely the number of IGV ω_1, the number of moving vane ω_2, the number of OGV ω_3, hub ratio ω_4, IGV and moving vane spacing ω_5, moving vane and OGV spacing ω_6, blade top clearance ω_7, IGV bending angle ω_8, IGV chord length ω_9, moving vane bending angle ω_{10}, moving vane swept angle ω_{11}, OGV bending angle ω, OGV chord length ω_{13}, fan diameter ω_{14}, were analyzed by the Sobol' global sensitivity analysis method. The analysis procedure is specifically displayed in Figure 8 and the schematic diagram of structural parameters is shown in Figure 9.

The global sensitivity values of each parameter to the total pressure and noise of the fan were obtained, as illustrated in Figure 10. In general, the influence of parameters such as IGV bend angle ω_8, IGV and moving vane spacing ω_5, and IGV chord length ω_9 was greater, among which moving vane bend angle ω_{10} and IGV bend angle ω_8 had the highest total global sensitivity values to pressure, which were 31.214% and 30.113%, respectively, and IGV bend angle ω_8 and IGV and moving vane spacing ω_5 had the highest total global sensitivity values to noise, which were 33.124% and 30.145%, respectively.

According to the above analysis, IGV and moving vane had a large impact while OGV had a relatively small impact on the aerodynamic performance and noise. The internal flow
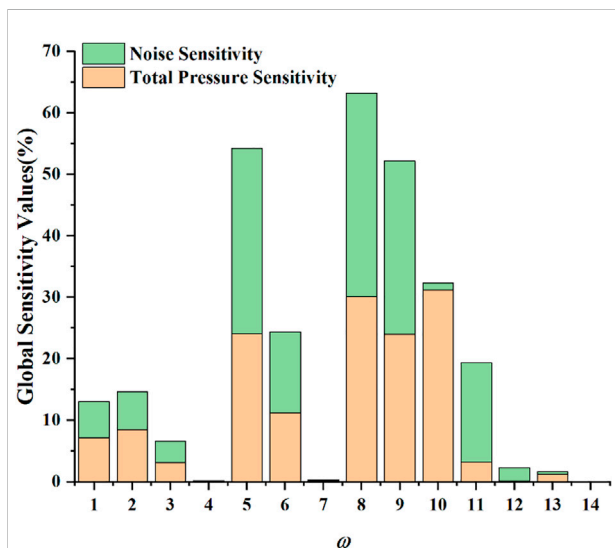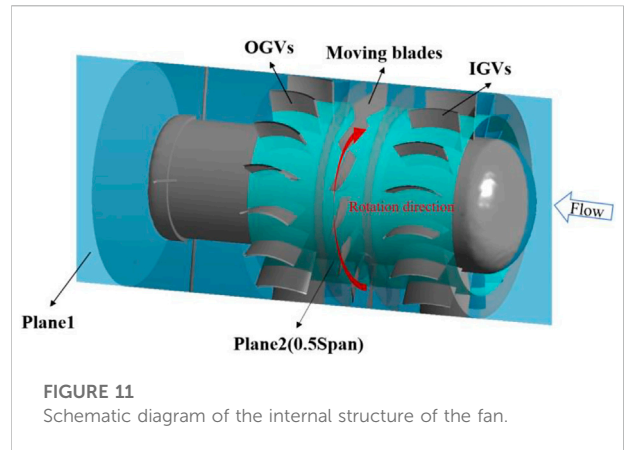

FIGURE 11
Schematic diagram of the internal structure of the fan.

characteristics of the fan will be analyzed as follows to further clarify the optimization objective.

3.2 Analysis of the internal flow characteristics of the fan

The radial section of the hub with blade flow surface $R = 280$ mm (0.5 times the blade height, Plane1) was selected to study the internal flow characteristics of the fan, and a vertical section was made over the center of the fan circle (as shown in Plane 2). Figure 11 shows the schematic diagram of the radial section of the hub.

Figure 12 shows the velocity vector distribution on Plane 1. As shown in the figure, there was an obvious vortex in the IGV area, which was located between the IGVs. The vortex was mainly concentrated on the pressure surface of the IGV, which was attributable to the blade shape of the guide vane. At the same time, there was a low-speed region in the reflux area, while a high-speed region on the suction surface of the moving blade, which resulted in flow disorder in the dynamic-static coupling zone between the IGV and the moving vane.

As a part of the fan, IGV deflected the air flow before entering the hub, increased the flow rate and pressure drop. It was hence an important part of a large axial flow fan. The above analysis also indicates that the structural design of the IGV was not rational and had a significant impact on the performance and noise of the fan, so IGV was identified as the optimization objective of this study.

4 Kriging multi-objective optimization

4.1 Parameterization

The IGV of axial fan is composed of blades with the same thickness. Its shape is formed by thickening and lofting the
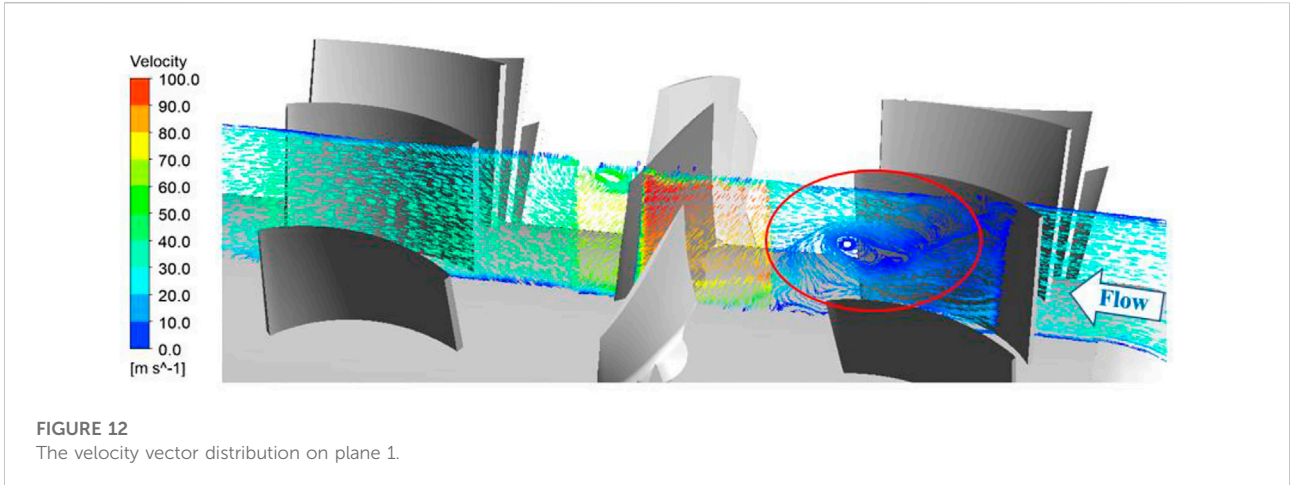

FIGURE 10
Summary of global sensitivity.

FIGURE 12
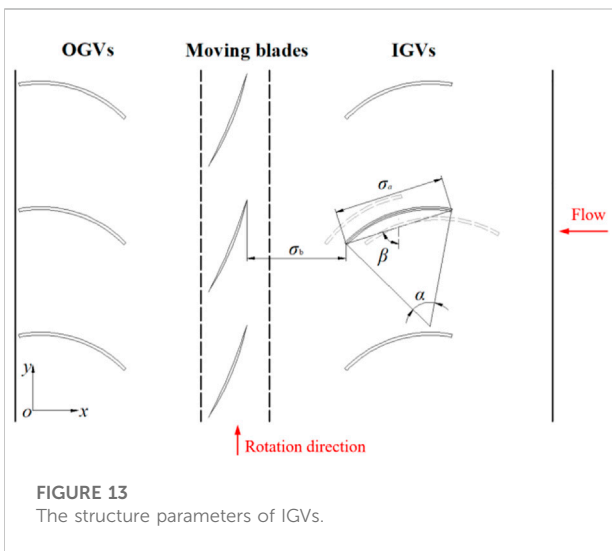The velocity vector distribution on plane 1.

FIGURE 13
The structure parameters of IGVs.

midline of the blade profile, and the midline is determined by controlling the arc length of a circle with radius R.

The parameters of the IGV are shown in Figure 13. The IGV midline was determined by chord length σ_a, angle α corresponding to the chord, tip deflection angle was defined as β, and the axial distance from the nearest point of the IGV midline to the leading edge of the moving vane as σ_b. These four parameters were optimized in this study.

A single circular arc blade is generally adopted in the nuclear power fans. The new IGV midline can be obtained by controlling parameter change and characterizing profile change. Under the premise of ensuring the smooth curvature of the blade, the variable range of each parameter is determined as follows: σ_a: 234–350 mm, α: 44–68°, β: 58–86°, σ_b: 208–312 mm.

4.2 Kriging model and optimization

Kriging model is an unbiased estimator with minimum variance. The design variables $x_i \in X = [x_1, x_2, \cdots, x_n]^T$ and response values $y_l \in Y = [y_1, y_2, \cdots, y_n]^T$ were assumed to follow a standard normal distribution. The unbiased estimation y_l^* of the random inputs x_i corresponding to y_l is shown as:

$$y_l^* = f(x)^T \beta_{:,l} + z_l(x), \quad l = 1, 2, \cdots, q \tag{11}$$

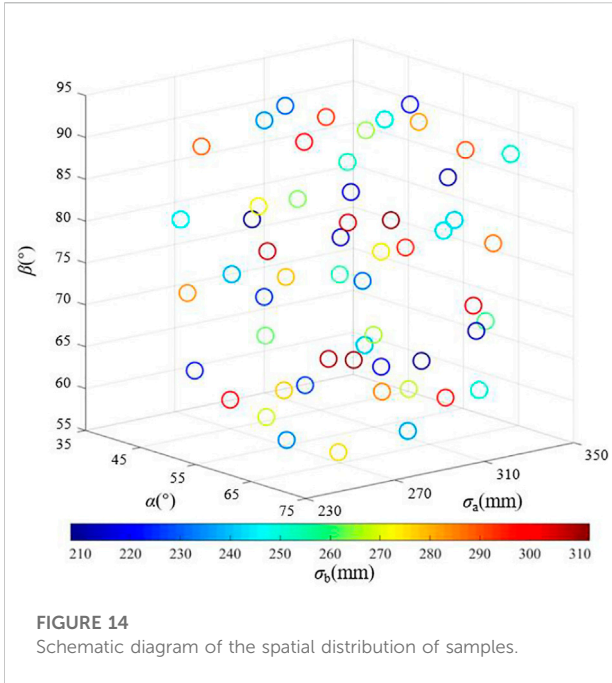$$\beta_{:,l} = \left(F^T R^{-1} F\right)^{-1} F^T R^{-1} Y \tag{12}$$

$$\gamma^* = \frac{z_l(x)}{r(x)^T} = R^{-1}\left(Y - F\beta\right) \tag{13}$$

where $f(x)$ is a vector of regression function consisting of polynomials, l is the dimension of the corresponding values, and $\beta_{:,l}$ is the corresponding regression coefficient. $z_l(x)$ is a random variable with variance σ_l^2, which means that the value is zero. γ^* is the local correlation coefficient, $r(x)$ is a vector describing the local correlation, R is the correlation matrix between the random variables, and F is the sample matrix.

To establish the Kriging model, samples should be obtained through experimental design. The optimal Latin hypercube experiment design (Opt LHD) is generally adopted to overcome the deficiencies of random sample space selection and sample concentration in Latin hypercube method. And its formula is expressed as:

$$G_{(L)} = \sum_{i=1}^{N} \sum_{j=i+1}^{N} \frac{1}{\left\| x_i - x_j \right\|^2} \tag{14}$$

As shown in Figure 14, the optimal Latin overshoot method was used to establish 55 groups of spatial samples for the variation range of design parameters, among which the first 50 groups were used as samples to draw IGV profiles, of which the first 50 groups were used as samples to draw the IGV profiles.

FIGURE 14
Schematic diagram of the spatial distribution of samples.

$$R^2 = 1 - \frac{\sum\limits_{i=1}^{n} (y_i - \hat{y}_i)^2}{\sum\limits_{i=1}^{n} (y_i - \bar{y})^2} \qquad (18)$$

Figures 15, 16 are the fitting results of Kriging model and the mean square error (MSE) of fitting design variables with the optimized target total pressure and SPL, respectively. The MSE value was calculated according to the mean squared error MSE formula (Eq. 17) and the linear regression coefficient was determined by R^2 formula (Eq. 18), and it can be seen from the figures that the MSE value of noise was less than 0.1 and that of pressure was less than 0.15, verifying that the accuracy of the established Kriging model met the requirements.

The constructed Kriging model was solved by NSGA-II with the overall number being set to 100, the mutation probability to 0.01, the crossover probability to 0.8, and the number of iterations to 400. The Pareto-front is shown in Figure 17, and the optimal solutions are listed in Table 2.

To verify the accuracy of the model optimization results, the obtained optimization results were brought into the model to recalculate the MSE, as shown in Table 3. As can be seen from the table, MSE was reduced significantly, indicating that the mean and variance of the obtained results were reduced to meet the design requirements and complete multi-objective optimization.
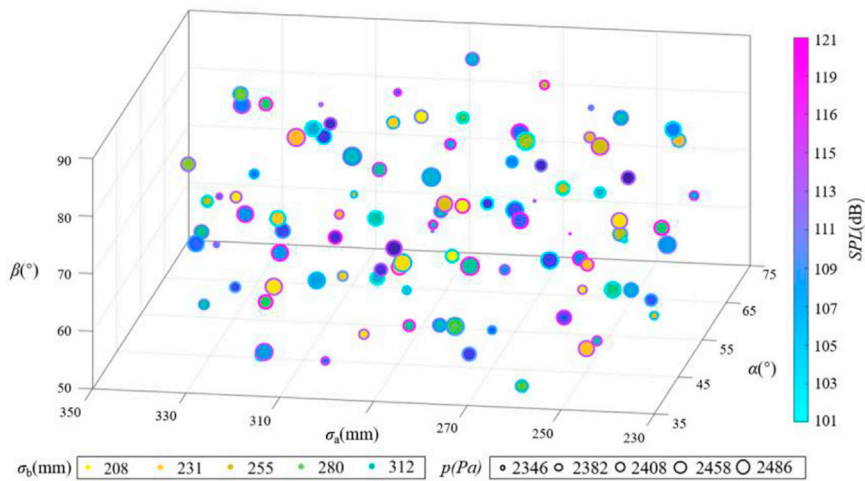
4.3 Optimization result and model

Figure 18 shows the settings optimization of IGV. The chord length σ_a of the IGV was increased by 55 mm, the corresponding circular angle α by 5°, the nearest distance σ_b from the IGV to the moving vane by 48 mm, and its angle with the y-axis β by 3°. The physical models are compared in Figure 19.

5 Comparison before and after optimization

5.1 Simulation result before and after optimization

To study the internal flow characteristics of the optimized fan, three planes were intercepted in the hub radial direction along the blade height located at R = 150 mm (10% blade height), R = 280 mm (50% blade height) and R = 430 mm (90% blade height) in the hub radial direction. The rotary surface is shown in Figure 20.

Figure 21 shows the streamlines at the blade heights of 0.1, 0.5, and 0.9 of IGV obtained by numerical simulation before and after optimization. It can be seen from the figure that vortices were more evident at the blade heights of 0.1, 0.5 and 0.9 and

It can be seen from the figure that the resulting samples were evenly distributed and well filled in space.

This study involves a typical multi-objective optimization problem. In order to seek the optimal solution and reduce the computational time while ensuring accuracy, the model was optimized by NSGA-II based on the fast non-dominated sorting method to reduce the computational amount while retaining excellent individuals, and the elite strategy was introduced to ensure the accuracy of the optimization results. In addition, crowding degree and crowding degree comparison operator are used to overcome the defects of NSGA that need to manually specify the sharing parameters while ensuring population diversity.

The IGV chord length σ_a, rounding angle α, tip deflection angle β, and the shortest axial distance σ_b between the IGV and the moving vane were taken as design variables, and the total pressure and noise of the fan as the optimization objectives. The corresponding mathematical model is:

$$\begin{cases} & Max\left(P\left(\sigma_a, \alpha, \beta, \alpha_b\right)\right) \\ & Min\left(SPL\left(\sigma_a, \alpha, \beta, \alpha_b\right)\right) \\ s.t. & 234 \le \sigma_a \le 350 \\ & 44 \le \alpha \le 68 \\ & 57 \le \beta \le 86 \\ & 208 \le \alpha_b \le 312 \end{cases} \qquad (15)$$

The constraint is:

$$\begin{cases} Q = 82400 \\ SPL \le 111.7 \end{cases} \qquad (16)$$

$$MSE = \sum_{i=1}^{n} \frac{1}{n} \left(f\left(x_i\right) - y_i\right)^2 \qquad (17)$$

FIGURE 15
Kriging model fitting results of design variables and total pressure and SPL.
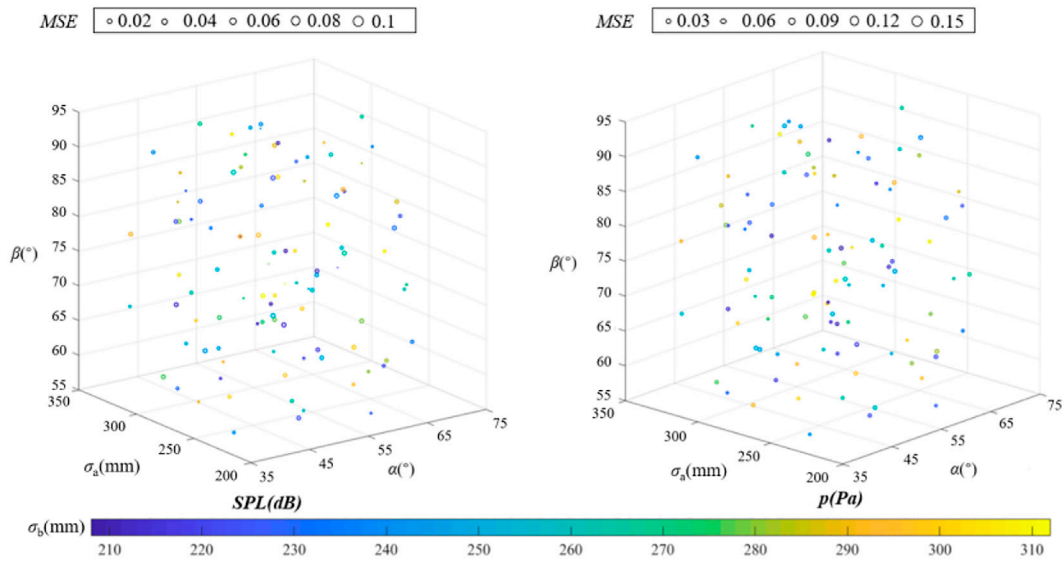
FIGURE 16
Fitted mean square error MSE.

were only present at the blade height of 0.1. After optimization, the vortex disappeared on the IGV and OGV at each blade height, but still accompanied by a low-speed region. Based on the results of the simulated internal flow field, the optimization effect was satisfactory and the proposed method was reliable to some extent.

The static pressure distributions at the blade heights of 0.1, 0.5 and 0.9 of IGV obtained by numerical simulation are shown in Figure 22. C_P is the pressure coefficient. Eq. 13 gives the C_P empirical formula (Clancy, 1975):

$$C_P = \frac{p - p_\infty}{\frac{1}{2}\rho_\infty V_\infty^2} \tag{19}$$

where p is the static pressure at the point of the required pressure coefficient, p_∞ is the static pressure away from any disturbance, ρ_∞ is the fluid density, V_∞ is the fluid velocity.
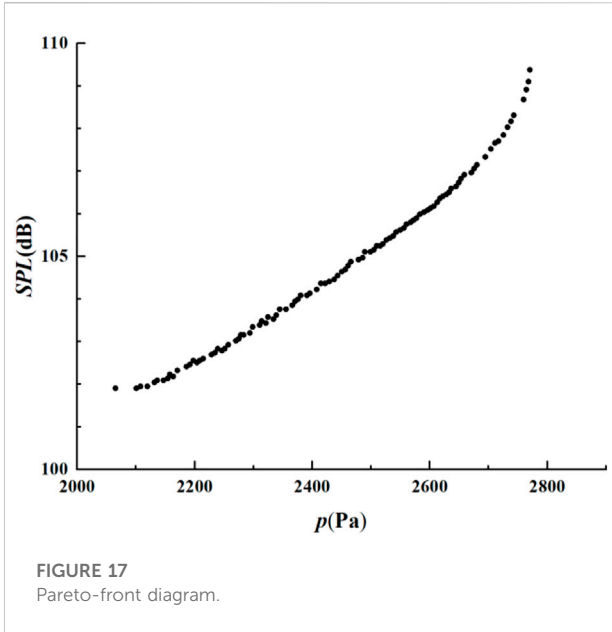
FIGURE 17
Pareto-front diagram.

TABLE 2 Comparison of parameters before and after optimization.

	σ_a (mm)	α (°)	β (°)	σ_b (mm)
Original	292	56	72	260
Optimization	298	61	76	310

TABLE 3 MSE before and after optimization.

		MSE
Original	SPL	0.043479
	p	0.089457
Optimization	SPL	0.023542
	p	0.033764

It can be seen that from Figure 22 the pressure coefficients of each blade height of the original IGV showed the same trend, but the pressure gradients were larger, and the separation points were all located before 0.2. In the interval of 0–0.2, the pressure surface C_p dropped from about 0.52 to about 0.18, indicating the possible presence of shedding vortices in such interval. After optimization, pressure coefficient amplitude increased, pressure gradient decreases, and the separation point was shifted back, suggesting that the pressure on the IGV surface changed more smoothly and the shedding vortex was reduced, which further reduced noise caused by the pressure fluctuation on the IGV surface. In addition, the optimized airflow kinetic energy decreased, the pressure of the fan increased, and the aerodynamic performance and efficiency were subsequently improved.

The numerical simulation results before and after optimization are shown in Figure 23. From Figure 23A, it can be found that the total pressure and efficiency at all flow rates were improved after optimization. At the flow rate of >70,000 m³/h, the total pressure increased more significantly by about 140.97 Pa at the design working condition, and at the flow rate of <85,000 m³/h, the efficiency of the fan at the design working condition was more obviously improved by about 2.06%. Moreover, the noise of the optimized fan at all flow rates at the at the design working condition was significantly reduced by about 3.08 dB.

5.2 Experimental result before and after optimization

The aerodynamic performance of the axial flow fan was tested based on the provisions and requirements of the "GB/T 1236–2017 standardized air duct performance test for industrial ventilators on air ducts". The settings diagrams of air performance test and field experiment have been mentioned in Section 2.2.

The aerodynamic performance curve of the fan before and after optimization is shown in Figure 24. It can be seen from the
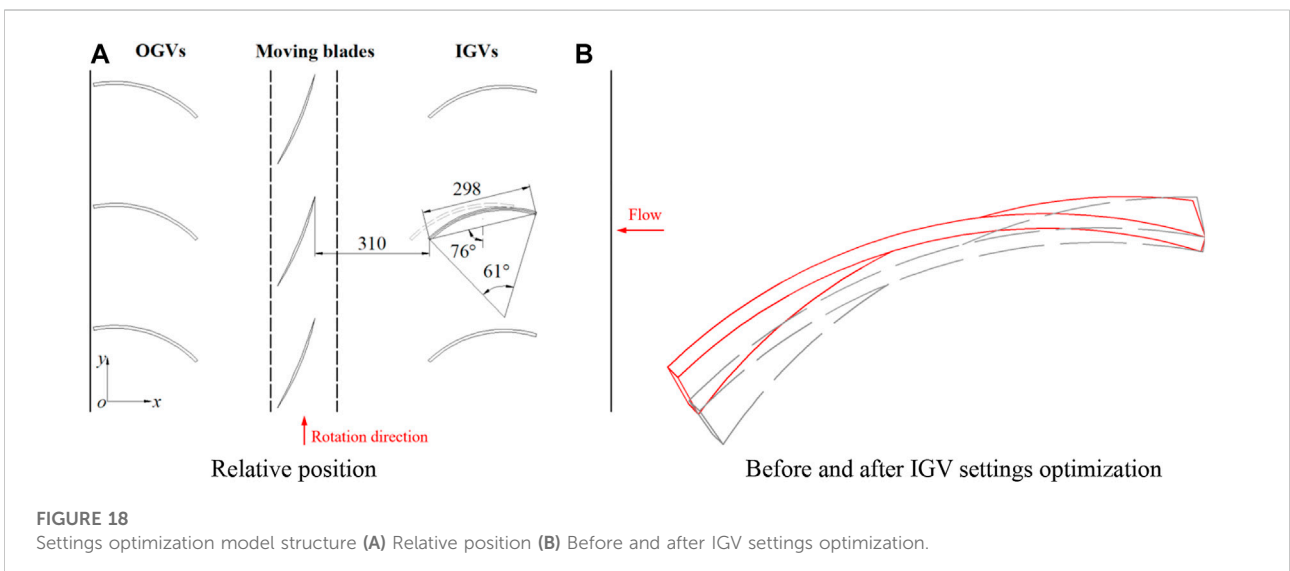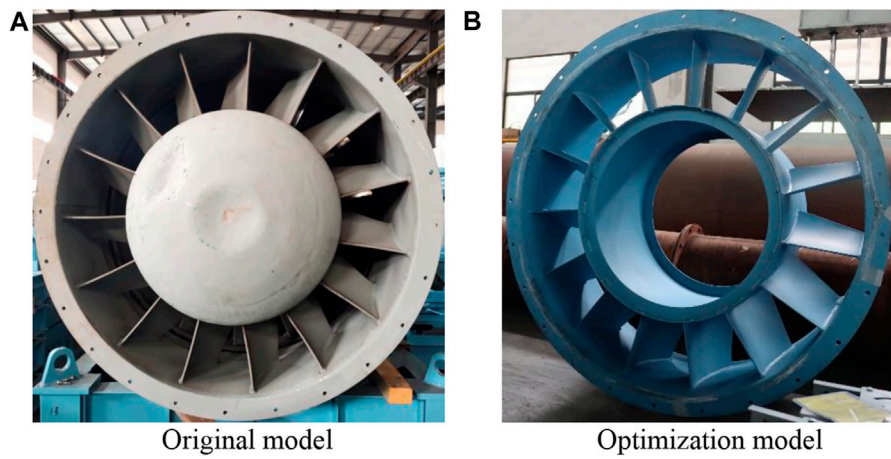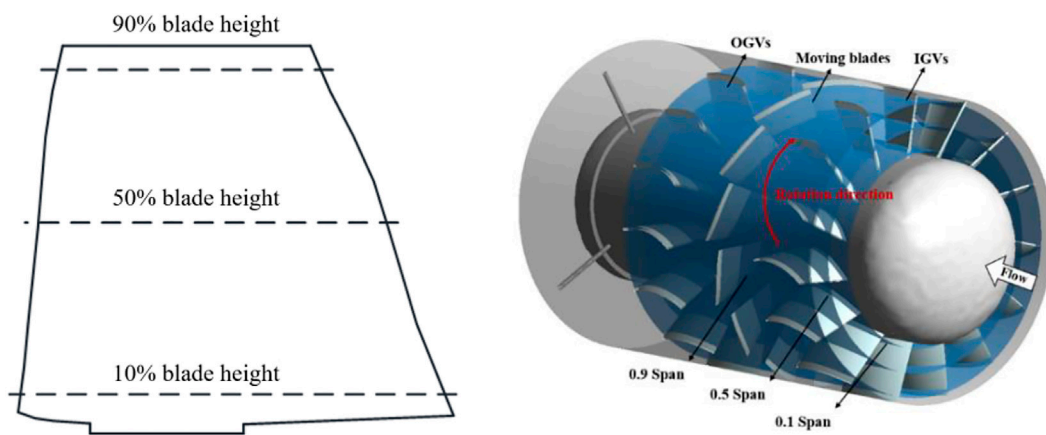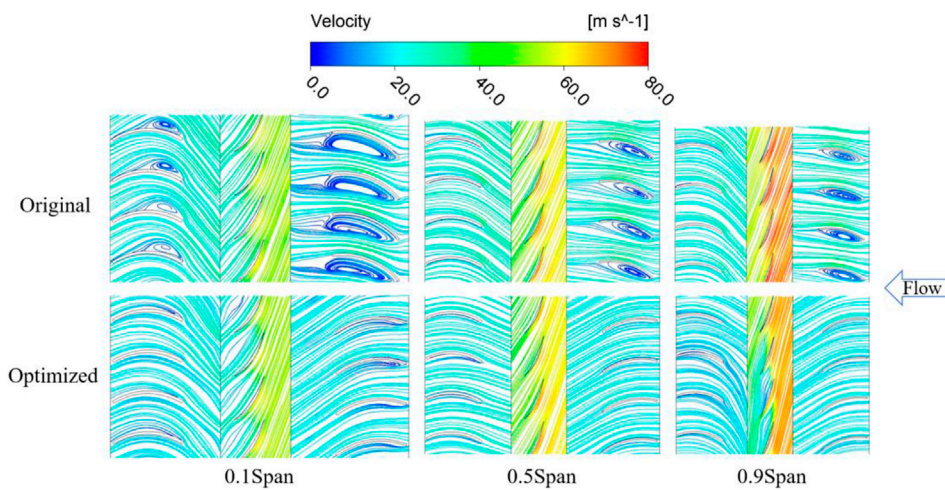

FIGURE 18
Settings optimization model structure **(A)** Relative position **(B)** Before and after IGV settings optimization.

FIGURE 19
Comparison of original and optimized models **(A)** Original model **(B)** Optimization model.

FIGURE 20
Schematic diagram of the rotating surface.

FIGURE 21
Streamlines coloured by flow velocity at different spans.

FIGURE 22
IGVs pressure distribution before and after optimization **(A)** Original **(B)** Optimization.

FIGURE 23
Numerical simulation results of aerodynamic performance before and after optimization **(A)** Performance **(B)** Noise.
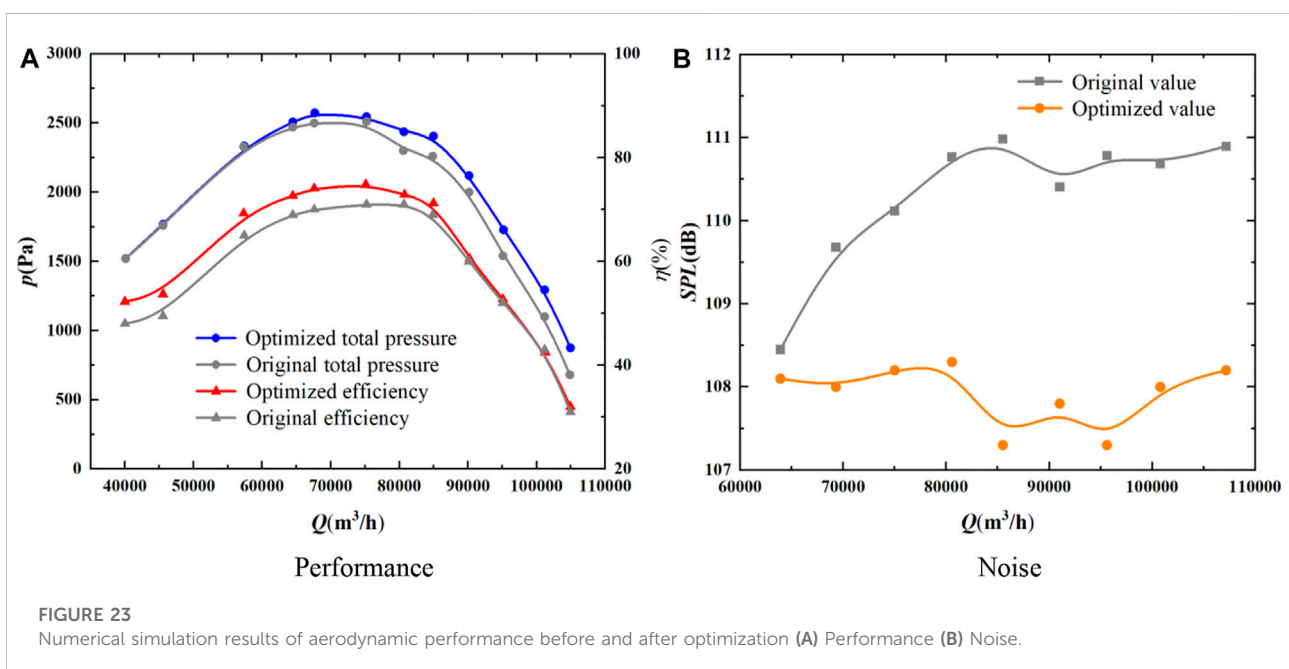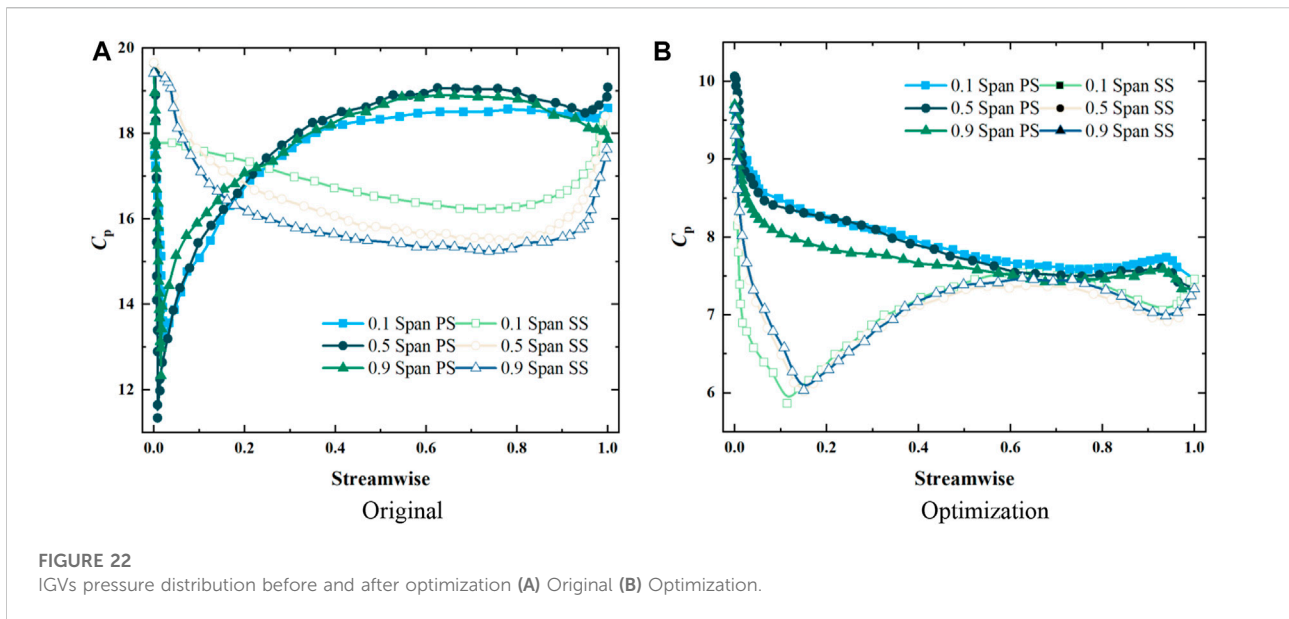
figure that the fan had the same trend in terms of aerodynamic performance before and after optimization, but the total pressure and total pressure efficiency of the optimized fan under various working conditions were much higher. The total pressure, static pressure and efficiency of the fan was respectively increased by 220.3 Pa, 257.8 Pa and 4.2% at most

after optimization. At the design operating point (82,400 m³/h), the total pressure of the fan was increased by about 156.4 Pa, the static pressure by 231.2 Pa, and the efficiency by about 0.86%. The increase in total and static pressure enabled the fan to overcome greater resistance, and the increase in efficiency reduced motor power and saved energy.
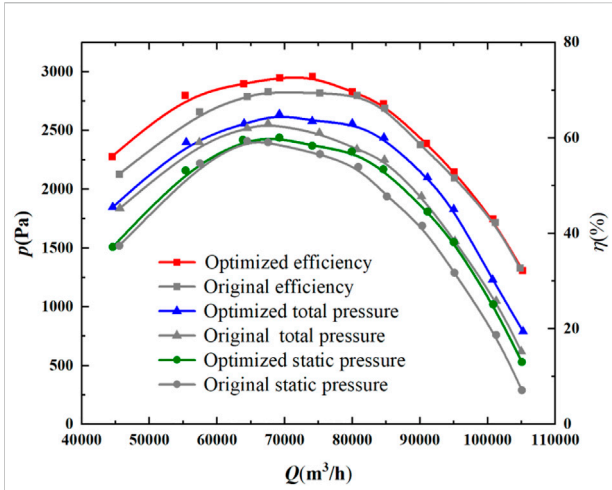
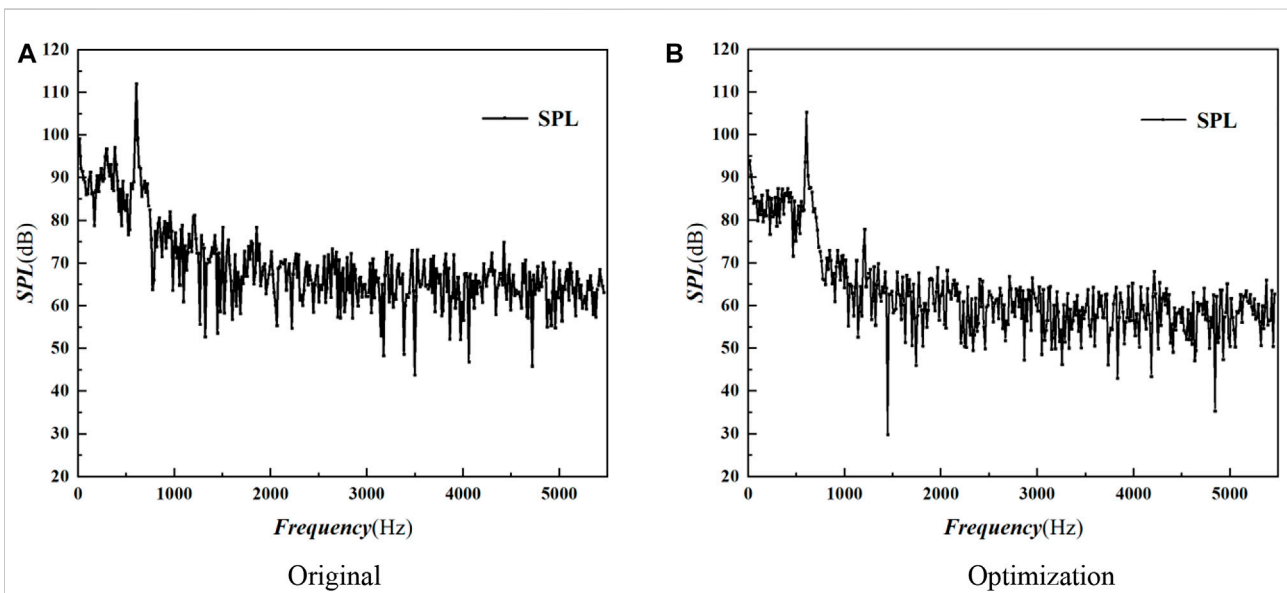**FIGURE 24**
Comparison of aerodynamic performance curves of fans before and after optimization.

Referring to the noise test standard "GB/T 2888-2008 fan and roots fan noise measurement method", noise receiving points were set at 45° from the center of the outlet surface, one time that of the diameter (1250 mm) at a horizontal position, and the noise of the optimized fan was also tested.

The SPL at the far-field noise receiving point of the original and optimized fans at the frequency of 0–5500 Hz were compared, as shown in Figure 25. Before and after optimization, the SPL spectrum distribution peaked at the motor operating frequency (14 Hz), fundamental frequency (302 Hz) and double fundamental frequency (604 Hz), and gradually decreased, which was the noise of the fan was converted from discrete to turbulent in such frequency range. And discrete noise in the fan contributed less to the far-field noise than turbulent broadband noise. After optimization, the peak value of the fundamental frequency dropped from 111.7 dB to 105.3 dB.

The noise values of the original and optimized IGV structures under different operating conditions are presented in Table 4. It can be found from the table that noise was significantly reduced under different operating conditions. The SPL of the optimized fan

FIGURE 25
Comparison of noise spectrum before and after optimization of large axial fan **(A)** Original **(B)** Optimization.

TABLE 4 Noise values under different working conditions in the test.

Working condition	Volume flow (m³/h)	Original *SPL* (dB)	Optimized *SPL* (dB)	Optimization values (dB)
1	63,874	110.8	105.3	5.5
2	69,141	110.9	105.2	5.7
3	73,969	111.3	105.3	6.0
4	80,568	111.3	105.2	6.1
5	84,489	111.7	105.3	6.4
6	90,957	111.5	105.3	6.2
7	94,960	111.6	105.5	6.1
8	100,659	111.6	105.4	6.2
9	107,056	111.7	105.6	6.1

operating at the low flow rate was reduced by 5.5 dB. With the increase of air volume, the SPL gradually decreased, and when the air volume exceeded 70,000 m³/h, the SPL of the fan gradually stabilized. At the design working point, the SPL of the fan was reduced by about 6.4 dB, indicating satisfactory optimization effect, which confirmed the reliability of the optimization method.

6 Conclusion

This study performed multi-objective optimization on an IGV for a large axial fan based on NSGA-II, and verified its feasibility and effectiveness through experiments and numerical simulations. The main conclusions of this work are as follows.

1) Using Sobol' global sensitivity analysis method, IGV bending angle and moving blade bending angle have the maximum sensitivity to the total pressure of the fan, and the distance between the IGV and the moving blade has the maximum sensitivity to noise. According to the analysis on the internal flow characteristics of the fan, there is obvious vortex between IGVs and the vortex is mainly concentrated on the pressure surface of IGVs.

2) The IGV pressure distribution before and after optimization was analyzed by numerical simulation. The results indicate that the static pressure gradient of the fan after optimization changed more smoothly and the shedding vortices were reduced. The experimental results confirm that the performance of the fan under various working conditions is improved after optimization, and the total pressure is increased by about 156.4 Pa and the total pressure efficiency by about 0.85% while noise is reduced by 6.4 dB.

3) In this study, the NSGA-II optimized Kriging model was applied to the multi-objective optimized design of a large axial fan IGV. The feasibility of the method was verified

and new ideas were provided for the optimal design of other large axial fans.

Data availability statement

The original contributions presented in the study are included in the article/supplementary material, further inquiries can be directed to the corresponding author.

Author contributions

SZ (First Author and Corresponding Author) and TZ participated in the design of this study, and they both perfoemed the statistical analysis. SZ carried out the study and collected important backgroud information. TZ drafted the manuscript. ZM and LL carried out the concepts, design, definition of intellectual content, literaturesearch, data acquisition, data analysis and manuscript preparation.

Conflict of interest

The authors declare that the research was conducted in the absence of any commercial or financial relationships that could be construed as a potential conflict of interest.

Publisher's note

References

Canepa, E., Cattanei, A., Mazzocut Zecchin, F., Milanese, G., and Parodi, D. (2016). An experimental investigation on the tip leakage noise in axial-flow fans with rotating shroud. *J. Sound Vib.* 375, 115–131. doi:10.1016/j.jsv.2016.04.009

Chai, X. Y., Xu, L. Z., Sun, Y. X., Liang, Z. W., Lu, E., and Li, Y. M. (2020). Development of a cleaning fan for a rice combine harvester using computational fluid dynamics and response surface methodology to optimise outlet airflow distribution. *Biosyst. Eng.* 192, 232–244. doi:10.1016/j.biosystemseng.2019.12.016

Chen, W., and Zhou, Y. (2021). Research on aerodynamic noise of tandem double cylinders based on K-fwh sound comparsion method. *J. Beijing Univ. Aeronautics Astronautics* 47, 10.

Choi, Y. S., Kim, Y. I., Kim, S., Lee, S. G., Yang, H. M., Lee, K. Y., et al. (2019). "A study on improvement of aerodynamic performance for 100HP axial fan blade and guide vane using response surface method," in ASME-JSME-KSME Joint Fluids Engineering Conference, San Francisco, California, USA, July 28–August 1, 2019 (New York: Amer Soc Mechanical Engineers).

Clancy, L. J. (1975). *Aerodynamics*. London: Pitman Publishing Limited.

Cui, L. J., Lu, Z. Z., and Zhao, X. P. (2010). Moment-independent importance measure of basic random variable and its probability density evolution solution. *Sci. China Technol. Sci.* 53 (4), 1138–1145. doi:10.1007/s11431-009-0386-8

Fakhraei, A., Faghihi, F., Rabiee, A., and Safarinia, M. (2021). Coolant flow rate instability during extended station blackout accident in NuScale SMR: Two approaches for improving flow stability. *Prog. Nucl. Energy* 131, 103602. doi:10.1016/j.pnucene.2020.103602

General Administration of Quality Supervision (2008). "Standardization administration of the people's republic of China," in *GB/T 2888-2008 Noise measurement method for fans and Roots blowers* (Beijing: China Standard Press).

General Administration of Quality Supervision (2017). "Standardization administration of the people's republic of China," in *GB/T 1236-2017 Standardized air duct performance test for air duct industrial ventilator* (Beijing: China Standard Press).

Gu, Z. Y., Zhu, Y. Y., Xiang, J. L., and Zeng, Y. (2021). A prediction method of operation trend for large axial-flow fan based on vibration-electric information fusion. *J. Cent. South Univ.* 28 (6), 1786–1796. doi:10.1007/s11771-021-4629-6

Hart, J. L., and Gremaud, P. A. (2018). AN approximation theoretic perspective of sobol' indices with dependent variables. *Int. J. Uncertain. Quantif.* 8 (6), 483–493. doi:10.1615/Int.J.UncertaintyQuantification.2018026498

Hu, Z. H., and Lu, W. (2017). "Numerical investigation on performance and aerodynamic noise of high speed axial flow fans," in 2nd IEEE Advanced Information Technology, Electronic and Automation Control Conference (IAEAC), Chongqing, China, 25-26 March 2017, 885–889.

Huang, W. H., Chen, L., Wang, W. J., Yang, L. J., and Du, X. Z. (2020). Cooling performance optimization of direct dry cooling system based on partition adjustment of axial flow fans. *Energies* 13 (12), 3179. doi:10.3390/en13123179

Kim, J. H., Ovgor, B., Cha, K. H., Kim, J. H., Lee, S., and Kim, K. Y. (2014). Optimization of the aerodynamic and aeroacoustic performance of an axial-flow fan. *Aiaa J.* 52 (9), 2032–2044. doi:10.2514/1.J052754

Kromer, F. J., Moreau, S., and Becker, S. (2019). Experimental investigation of the interplay between the sound field and the flow field in skewed low-pressure axial fans. *J. Sound Vib.* 442, 220–236. doi:10.1016/j.jsv.2018.10.058

Moaveni, B. S. (1999). *Finite element analysis theory and application with ANSYS.* New Jersey, United States: Prentice-Hall.

Nishi, Y., Mori, N., Yamada, N., and Inagaki, T. (2022). Study on the design method for axial flow runner that combines design of experiments, response surface method, and optimization method to one-dimensional design method. *Renew. Energy* 185, 96–110. doi:10.1016/j.renene.2021.12.009

Taghinezhad, J., Alimardani, R., Masdari, M., and Mahmoodi, E. (2021). Performance optimization of a dual-rotor ducted wind turbine by using response surface method. *Energy Convers. Manag. X* 12, 100120. doi:10.1016/j.ecmx.2021.100120

Tanasic, N., Jankes, G., and Skistad, H. (2011). Cfd analysis and airflow measurements to approach large industrial halls energy efficiency: A case study of a cardboard mill hall. *Energy Build.* 43 (6), 1200–1206. doi:10.1016/j.enbuild.2010.12.034

Tang, X., Luo, J. Q., and Liu, F. (2017). Aerodynamic shape optimization of a transonic fan by an adjoint-response surface method. *Aerosp. Sci. Technol.* 68, 26–36. doi:10.1016/j.ast.2017.05.005

Venturelli, G., and Benini, E. (2016). Kriging-assisted design optimization of S-shape supersonic compressor cascades. *Aerosp. Sci. Technol.* 58, 275–297. doi:10.1016/j.ast.2016.08.021

Zhang, C., Li, A. G., Li, J. X., Hou, Y. C., and Chen, X. (2021a). Radiation noise control of a 90° rectangular elbow in ventilation and air conditioning systems. *J. Build. Eng.* 37, 102157. doi:10.1016/j.jobe.2021.102157

Zhang, S. G., Li, R. Z., Zhang, Y. F., and Chen, H. X. (2021b). Aerodynamic optimization and noise reduction of a two-stage series compact fan. *J. Aerosp. Eng.* 34 (5). doi:10.1061/(asce)as.1943-5525.0001304

Zhang, W. J., Yuan, J. P., Zhou, B. L., Li, H., and Yuan, Y. (2018). The influence of axial-flow fan trailing edge structure on internal flow. *Adv. Mech. Eng.* 10 (11), 168781401881174. doi:10.1177/1687814018811745

Zhao, F. T., Jing, X. D., Yang, M. S., Wang, D. Y., Sha, Y. D., and Luan, X. C. (2020). Experimental study of rotor blades vibration and noise in multistage high pressure compressor and their relevance. *Chin. J. Aeronautics* 33 (3), 870–878. doi:10.1016/j.cja.2019.02.008

Zhou, S. Q., Hu, Y. J., Lu, L. F., Yang, K., and Gao, Z. L. (2022). IGV optimization for a large axial flow fan based on MRGP model and Sobol' method. *Front. Energy Res.* 10. doi:10.3389/fenrg.2022.823912

Nomenclature

Variables

D Diameter (mm)

E Mathematical expectation

F Sample matrix

I_F Failure indicator function

m_1 Number of IGVs

m_2 Number of OGVs

n Rotaing speed(r/min)

p_{tf} Total pressure(Pa)

Q The fan volume flow(m³/h)

r Vector of local correlations

R^2 Linear regression coefficient of determination

S_i Global Sensitivity Indicator

V (·) Variance Operator

x_i Random Variable

$y+$ A dimensionless parameter

y_l Response

Z Number of moving blade

z_l Random variables

Greek letters

α Central angle

β Guide vane tip deflection angle

$\beta_{:,l}$ Regression coefficients

$\gamma^\star$ Local correlation coefficient

σ_a The chord length of the guide blade(mm)

σ_b The distance between moving blade and IGVs (mm)

σ_l^2 Variance

ω_i Structure parameters

Abbreviations

CFD Computational Fluid Dynamics

$FW\text{-}H$ Ffowcs Williams and Hawkings

$GERSM$ Gradient-Enhanced Response Surface Model

IGV Inlet guide blade

MSE Mean Square Error

$NSGA\text{-}II$ Non-dominated Sorting Genetic Algorithm-II

OGV Outlet Guide Blade

$Opt\ LHD$ Optimal Latin hypercube design

SPL SPL (dB)